ON THE INTERACTION OF WATER DROPLET WITH A SHOCK WAVE: EXPERIMENT AND NUMERICAL SIMULATION

Sergey V. Poplavski[a], Andrey V. Minakov[b,c,*], Anna A. Shebeleva[b,c], Viktor M. Boyko[a]

[a]Khristianovich Institute of Theoretical and Applied Mechanics SB RAS, Novosibirsk, 630090, Russia

[b]Siberian Federal University, Krasnoyarsk, 660041, Russia

[c]Kutateladze Institute of Thermophysics SB RAS, Novosibirsk, 630090, Russia

Corresponding author. E-mail address: tov-andrey@yandex.ru (A.V. Minakov)

ABSTRACT

The work is devoted to experimental and computational studies of the behavior of water drop in a flow behind incident shock wave and verification of calculations on this basis. In the experiments, a high-speed visualization of the water drop interaction with the flow behind incident shock wave was obtained at shock wave Mach numbers Ms=1.109-1.34 and Weber numbers We = 200 - 2200. The calculations simulate conditions of the experiments and are based on the use of the volume of fluid (VOF) method to resolve the phase interface, large eddy simulation (LES) model to describe turbulence, as well as adapted dynamic grid technology. The structure of the flow near and in the wake of a drop, the features of the flow around a drop, the type of the shape evolution, and the character of the mass entrainment were studied. Comparison of simulation results with experimental data has shown good agreement with respect to main integral characteristics of the process, i.e. morphology, dynamics, and induction time of droplet breakup.

Keywords: the aerodynamic breakup of drops, shock waves, mathematical simulation, VOF, LES.

1. Introduction

Aerodynamic crushing of droplets is widely used in various industries, such as energy, aircraft, and rocket engine building, hardening of materials and coatings, chemical industry, etc. Aerodynamic mechanisms are most effective in flows with high parametric gradients, while the interaction of droplet with pressure jumps and incident shock waves (SW) are the limiting cases of gradient flows. In the technogenic systems, the interaction of droplets with SW takes place, for example, in close proximity to airframe components of the supersonic aircraft *Ranger et al. (1969).* Thunderstorm processes in the precipitation zone, causing large-scale changes in the atmosphere, are also accompanied by the propagation of shock waves in the gas-droplet medium.

The study of droplets dynamics and breakup in the flow behind incident SW holds a special place in the subject of the aerodynamic dispersion of liquids by *Boiko et al. (1987)* and *Gelfand et al. (1974)*, and since the early works, has developed in two directions. First, this issue concerns the problems related to the combustion of the hydrocarbon fuel aerosols in relation to industrial explosion safety by *Boiko et al. (1974, 1991); Gelfand et al. (1974, 1978)* and to advanced Pulse Detonation Engines (PDE) by *Dinh (2003)*. The process takes place in two stages: first, droplets breakup behind the SW; and second, ignition of the mixture and the movement of the flame front over the spray. The risk of explosion increases in the case of supersonic flow behind the SW front. Here, the conditions arise that accelerate the self-ignition of the flammable spray – the increase in gas pressure and temperature during flow deceleration in two phase mixture by *Boiko et al. (1993)*.

Since spraying proceeds equally for all low-viscosity liquids by *Boiko et al. (1974, 1991); Gelfand et al. (1974, 1978, 1996)* it can be studied with regard to water that as noted is of independent interest. Thus, the second direction appeared in the study of droplet behavior in SW, namely dynamics by *Boiko et al. (2007, 2009); Ranger et al. (1970);Ortiz et al. (2004)* and drop breakup mechanisms at a sudden penetration into the flow *Boiko et al. (2012); Gelfand et al. (1996, 1974); Theofanous et al. (2008)*. This became the most popular formulation of the problem from the experimental standpoint. This is due to the fact that only in SW the coordinate and the moment of the drop falling into the flow are precisely determined. At that, the visualization of the droplet deformation and the type of its breakup are the most informative to analyze the process itself. There are also hidden processes inside the drop that are not observable. However, all the ideas about the drop breakup are based only on the data on the nature of its deformation before beginning erosion of liquid surface and during it progression by *Boiko et al. (1987, 1991); Gelfand et al. (1974, 1978, 1996);*. The movement of the liquid boundary relative to the initial surface of the droplet due to the changing distribution of external pressure gives rise to the most bizarre shapes in different streamlining regimes. Attempts to establish a relationship between the droplet deformation and the external flow pattern were made in early works by *Ranger et al. (1970)* though, based on an essential simplification of the droplet shape considered as an ellipsoid of rotation with a small axis along the velocity vector. This type of deformation is possible for raindrop type regimes, i.e. freely falling droplet with a diameter of $d_0 \sim$ 2-3 mm and steady velocity of ~ 4-5 m/s. Though, the deformation type in the flow behind the SW is quite different, but the model of the conjugated boundary

layer formation in the liquid, proposed in *Ranger et al. (1970)*, is still relevant for liquid jets, films, and droplets *Gelfand (1996).*

Thus, crushing mechanisms are determined by processes on both sides of the phase interface. Such problems with the resolution of small-scale process are available only for numerical methods, and this is an important aspect to motivate computer simulation of the process. Verification of calculations based on experimental data will allow debugging the numerical technique and receiving the new data, which are inaccessible in experiments. An important task of numerical simulation, for both verification and research purposes, is the droplet morphology as a response of the liquid sphere to the change in the pressure distribution over the surface during restructuring the field of streamlining of the body with changing shape.

Returning back to the experiments, we should note that the possibility of detecting a droplet with reference to the moment of entering the flow behind the SW front, made shock tubes the most effective tool for this kind of research. That is why the experiments with droplets in SW were repeatedly reproduced in many laboratories around the world for a wide range of regimes that increase the reliability of the data collected in a number of reviews by *Gelfand (1996); Theofanous et al. (2008).* There are also unsolved problems associated with the development of innovative technologies and the creation of new materials with complex rheology. Thus, the interaction of droplets with shock waves is one fundamental problem of physical gas dynamics within the framework of the heat and mass transfer in non-equilibrium heterogeneous systems of technogenic and natural origin, while computer simulation of these processes is the relevant and promising research trend.

2. Physical mechanisms of the droplet breakup in shock wave

Aerodynamic breakup modes of low-viscosity liquid droplets are determined by the Weber criterion: the We number is the ratio of the disturbing flow force $\sim\rho u^2 d^2$ and the stabilizing surface tension force $\sim\sigma d$, i.e. We = $\rho u^2 d/\sigma$ *Gelfand et al. (1974, 1996)*, where ρ and u are the density and velocity of the gas, while d and σ are the droplet size and surface tension. There are the following six modes of drops breakup according to *Gelfand et al. (1974)*: vibrational breakup ($8 < We < 12$) (1), bag breakup ($12 < We < 50$) (2), bag-and-stamen breakup ($50 < We < 100$) (3), sheet stripping ($100 < We < 250$) (4), wave crest stripping ($We > 250$) (5), and catastrophic breakup ($We > 250$) (6).

Other classifications are also known. They differ in types of breakup and ranges in We numbers *Boiko et al. (1987); Gelfand et al. (1974).* For example, in *Boiko et al. (1987)* it is shown that the change of mechanisms 4 and 5 in SW occurs at We ~1000, rather than $We > 250$. The nominal differences between the classifications would not be important if they were not related to the relevant physical mechanisms. The point is that the traditional classifications are based on the droplet morphology, but in *Gelfand (1996)*, and later in *Theofanous et al. (2008)* it is proposed to define the droplet breakup types depending on the following physical mechanisms.

1. Types 1-3 are combined into one Rayleigh-Lamb-Taylor instability mode within the expected range of We numbers, $10 \le We \le 40$;
2. Types 4 and 5 represent the sheet stripping from the liquid surface layer occurring according to the boundary layer formation mechanisms (4) and the development of its instability (5) within the expected range of We numbers, $40 \le We \le 10^5$;

3. Type 6 is the catastrophic breakup as a consequence of Rayleigh-Lamb-Taylor instability development within an expected range of We numbers, $10^3 \leq We \leq 10^5$.

Currently, the numerical simulation of these processes is a rather challenging task. Here, the only universal tool is a direct numerical simulation (DNS) with full resolution of the phase interface, but because of the huge computational cost, this approach can be used only for a very narrow class of model problems. Alternatively, a technique based on a combination of the volume of fluid (VOF) method for resolving the phase interface, large eddy simulation (LES) models for describing turbulent flows, and dynamic grid technology adapted to the phase interface, can be employed as well. This approach is less demanding on computing resources and allows describing the behavior of the mobile phase interface at the main turbulent scales. However, it requires further development and testing for the application in applied problems. The most effective testing of numerical technology is conducting simulations in the same conditions as in the available experiments, and comparing the results by the maximum number of indicators, such as the following integral quantitative parameters:

- *droplet deformation rate by Boiko et al. (2007, 2009);*

- *the breakup induction period by Boiko et al. (2012);*

This may be the structural characteristics of the process:

- *the deformation scenario and peculiarities of droplet streamlining;*

- *the type of instability of the droplet surface and the nature of the mass entrainment by Boiko et al. (2012);*

The numerical simulation technique, verified by such a set of characteristics, will allow using calculations for a wide range of applications and to obtain new data are not available in experiments.

3. Experiment statement and analysis of observations

3.1. Experimental setup and diagnostics

The experiments were carried out using the UT-4M shock tube (Institute of Theoretic and Applied Mechanics of the Siberian Branch, Russian Academy of Sciences), which is described in detail in *Boiko et al. (1987, 1991)*. The installation is characterized by the following main features: the high-pressure chamber and the low-pressure channel are separated by an electro-valve to start the installation by means of a signal from the synchronization system; the low-pressure channel 5 m long allows obtaining a quasi-stationary flow behind the shock wave front during ~ 500-600 μs; the measuring section has a cross-section of 52x52 mm, equipped with quartz windows 20x200 mm in size to carry out shadow visualization, as well as a device for entering freely falling droplets. The installation is started by the synchronization system when a droplet enters the measuring section. The same device starts a registration system with the arrival of the shock wave front. Registration is carried out by a multi-frame shadow system with a laser stroboscopic light source. The following are some details about the visualization system.

When registering fast processes, dynamic spatial-temporal resolution is one of the main factors determining the choice of recording equipment and its operation mode. Despite the rapid development of electronic image registration, in the study of high-speed processes ($V \geq 10^3$ m/s), traditional photography still has advantages. In such experiments, optical-mechanical equipment is still widely used *Versluis (2013)*. High-

speed shooting (>10^3 fps) is performed on a static photo material, and the displacement of the rays along the photosensitive layer is performed by a scanning system with a rotating mirror or mirror prism. Separation of frames on a film (image switching) in cameras with a mirror scan of the constant light flux is performed using lens inserts.

The disadvantage of this kind of filming is the long exposure time of the frame τ_e relative to the interval between frames Δt, it is estimated at $\tau_e/\Delta t = 0{,}5 \div 1$. To reduce τ_e, it is necessary to increase the shooting frequency. But, for example, at a frequency of 625000 fps and a frame size of 10 mm τ_e = 1,6 μs. The object displacement during this time is too large (>1 mm). In order for the spatial displacement of the image of the process (or object) at a speed of ~ 10^3 m/s not to limit the limiting resolution of the optical system $R_o = 1/d \sim 2 \cdot 10^4$ m^{-1}, it is necessary to provide an exposure time of ~ $5 \cdot 10^{-8}$ s. This is two orders of magnitude less than the minimum shutter speeds for optical-mechanical cameras. Therefore, cameras with a mirror scan in the normal filming mode do not provide high quality registration of high-speed two-phase flows.

More promising is the method in which the exposure time, frequency and number of frames are set by a pulsed light source, and the optical-mechanical camera performs spatial separation of frames. The basic element of such a diagnostic complex is the stroboscopic ruby laser light source with periodic Q-switching by the Kerr cell developed at the Institute of Theoretic and Applied Mathematics (Siberian Branch of the Russian Academy of Sciences). Based on this source, various imaging methods are implemented, including shadow, schlieren, and other methods *Boiko et al. (1997, 2002); Gavrilenko et al. (1986)* with a frame rate of more than 3*10^4 fps and exposure time of 30 ns.

In this work, we used a shadow scheme with the stroboscopic ruby laser as a light source and recording onto a fine-grained film by the camera with a rotating mirror prism. Rotating prism, unlike a mirror, always reflects light into the angular sector, on which a 15-20 frames segment of the film is located, therefore the camera does not need synchronization with the process under study and is called a standby camera. The absence of the requirement to synchronize the survey with the shock tube start is an important feature of the experiment, because the arrival of the shock wave front occurs with a spread of > 1 ms from the moment the installation is started, but the entire process lasts only 0.5-0.6 ms. Therefore, the start of the light source is performed upon the arrival of the shock wave front into the measuring section at constant readiness of a recorder with a previously untwisted mirror prism. The interval between frames is 30±0.1 μs and the exposures of 30 ns are set by the light source.

3.2. Flow parameters behind a shock wave front

Shock waves parameters were calculated by the ideal theory of shock waves *Henshall (1957); Lapworth (1970)*, which gives high accuracy for Mach numbers of the shock wave $M_S = V_S/c \leq 4$, where V_S is the velocity of the shock wave front, c is the sound velocity in front of it. The value of Vs was measured twice: during the experiment, Vs was determined to synchronize the installation systems over the travel time between pressure sensors with an accuracy of 2%; when processing shadow images, Vs was determined from the position of the front on adjacent frames with a known interval between them with an accuracy of < 1%. In the experiments, the interaction of water droplets with shock wave was modeled at We numbers ranged from 200 to 2200. Figure 1 shows a series of shadow images of the process at Ms = 1.32, $We = 2 \cdot 10^3$, d_0 = 2.81 mm. Shock wave moves from left to right, the front of the shock

wave is visible on frame No. 1, and in the previous frame the front coincided with the left edge of the frame. Flow parameters behind the wave front: temperature T_2 = 354 K (81 C), density ρ_2 = 2.0 kg/m^3, and gas velocity u_2 = 162 m/s. Data from other experiments in this series are given in *Section 5*.

3.3. Preliminary Observation Analysis

In *Ranger et al. (1969)* it was proposed to describe the droplet dynamics in shock wave in terms of dimensionless quantities $X = x / d_0$ and $T = t / t_0$, where x is the longitudinal coordinate, t is the physical time, $t_0 = (d_0 / u_2)\cdot(\rho_l / \rho_2)^{0.5}$. According to numerous experiments, a universal dependence for the induction period of the mass entrainment was found, $t_i / t_0 \approx 0.35\pm0.4$. It was also argued that the acceleration of the droplet is constant up to $T \approx$ 6-8; then $X \approx kT^2$. Note that this dependence does not refer to the mass center of the droplet, but to the leading edge. Moreover, this dependence is quite approximate at the ambiguous influence of the midsection growth and the mass entrainment. Because of this the value of k differs markedly by different authors. Thus, according to *Ranger et al. (1969)* k = 0.71–1.1, according to k = 0.8 – 1.1. As shown in *Boiko et al. (2007, 2009)*, the droplet dynamics are much more complicated, the acceleration is not constant, and decreases sharply with the development of intense mass entrainment within the range $T \approx$1-3.

However, for a preliminary analysis we will also use estimates in dimensionless parameters. For conditions on Fig.1, t_0 = 387 μs, taking into account the residence time of the drop in the flow on frame No. 1 (22 μs), the total observation time of the droplet t_N = 412 μs (t_N / t_0 = 1.05). During this time the droplet has moved by the distance x=2.79 mm (x / d_0 = 0.99), the coefficient k = 0.9. Beginning of mass entrainment is seen on frame No. 5, the breakup delay (induction period) is t_i = 142±15 μs, while in

dimensionless form, $t_i / t_0 = 0.36$ that, similarly to coefficient k, is close to the accepted data on the interaction of the droplets with the shock wave.

The results of experiments conducted according to this technique are published in *Boiko et al. (1987; 1991; 1987; 2007; 2012)*. Analysis of the above experiment, as well as other experiments in this series, shows that in the accepted terms, all modes were implemented in the right conditions. They can serve a basis for verification of numerical technology in terms of both quantitative data, and, most importantly, graphical data on the morphology of droplet interacting with a shock wave. To date, these data are the most detailed of those obtained within the range of We numbers 200 - 2200, known in the literature.

4. A mathematical model of drop breakup in the flow behind incident shock wave

At present, a wide range of mathematical models, for example *Aggarwal (1995); Minakov (2014); Frank (2001),* is proposed to describe gas-droplet flows, which differ in the ways of describing the gas and particles motion, as well as used assumptions and restrictions. The choice of a suitable model is carried out, as a rule, taking into account the available information about the flow structure and the required accuracy of its description. The most complete reviews on methods for solving problems with moving contact boundaries are presented in *Hirt et al. (1981); Kothe D.B et al. (1996); Tavangar et al. (2015).*

Among the algorithms based on continuous volume markers, the most popular method due to the ease of implementation and efficiency is the volume of fluid (VOF) method *Hirt et al. (1981)*, which proved to be good when calculating free surface flow. The idea of the method is that liquid and gas are considered as a single two-component

medium, in which the spatial distribution of phases within the computational domain is determined by a special marker function F(x, y, z, t). The volume fraction of the liquid phase in the cell under consideration is taken as follows: F(x,y,z,t) = 0, if the cell is empty, F(x,y,z,t) = 1, if the cell is completely filled with liquid, and 0 < F(x,y,z,t) < 1, if the phase interface is within the cell. Since the free surface moves with the liquid, tracking the movement of the free interface is performed by solving the transfer equation of the liquid volume fraction in the cell:

$$\frac{dF}{dt} + V \cdot \nabla F = 0, \tag{1}$$

where V is the velocity vector of the two-phase medium, found from the solution of a system of hydrodynamics equations, i.e. the mass conservation or continuity equations:

$$\frac{d\rho}{dt} + \nabla(\rho \cdot V) = 0, \tag{2}$$

and motion equations or the momentum conservation law:

$$\frac{d\rho V}{dt} + \nabla(\rho V \times V) = -\nabla p + \nabla(\tau) + F, \tag{3}$$

Here τ is the viscous stress tensor, F is the volumetric force vector, $\boldsymbol{p}$ is the static pressure, $\boldsymbol{\rho}$ is the density of the two-phase medium. Components of viscous stress tensor τ_{ij} are written as:

$$\tau_{ij} = \mu\left(\frac{dU_i}{dx_j} + \frac{dU_j}{dx_i} - \frac{2}{3}\delta_{ij}\frac{dU_k}{dx_k}\right), \tag{4}$$

where μ is the dynamic viscosity of a two-phase medium, U_{ij} are the velocity vector components. The density and molecular viscosity of the considered two-component medium are found through the volume fraction of the liquid in the cell according to the mixture rule:

$$\rho = \rho_1 F + (1 - F)\rho_2 , \tag{5}$$

$$\mu = \mu_1 F + (1 - F)\mu_2 , \tag{6}$$

where ρ_1 and μ_1 are the density and viscosity of the liquid, ρ_2 and μ_2 are the density and viscosity of the gas. The obtained values of density ρ and viscosity μ are included in the motion equations and determine the physical properties of the two-phase medium.

When considering fluid flows with a free interface, special attention is paid to the surface tension phenomenon. The study of the flows driven by the surface tension forces is a very complex independent task. Therefore, the advantages of the VOF method also include the fact that it allows a relatively simple simulation of the effect of surface tension forces. Most often, the CSF algorithm *Brackbill et al. (1992)* is used to simulate the surface tension in the framework of the VOF method, which involves the introduction of an additional volumetric force, F_S into the motion equations, which is determined from the correlation:

$$F_s = \sigma k \nabla F , \tag{7}$$

where σ is the surface tension coefficient, k is the curvature of the free surface, which is defined as the divergence of the normal vector:

$$k = \nabla(\frac{n}{|n|}) , \tag{8}$$

The normal to the free surface is calculated, in turn, as the gradient of the volume fraction of the liquid phase in the cell:

$$n = \nabla F , \tag{9}$$

The simulation of turbulence is another important factor when calculating droplet breakup. In this paper, we used the LES model [24] *Smagorinsky (1963)* for turbulence modeling, according to which the solution of filtered Navier-Stokes

equations is necessary to describe turbulent flows. Then, the above-mentioned system of hydrodynamics equations can be rewritten in the following form:

– continuity equation:

$$\frac{\partial \rho}{\partial t} + \frac{\partial}{\partial x_i}\left(\rho \overline{u_i}\right) = 0, \tag{10}$$

– momentum conservation equations

$$\frac{\partial}{\partial t}\left(\rho \overline{u_i}\right) + \frac{\partial}{\partial x_j}\left(\rho \overline{u_i}\,\overline{u_j}\right) = \frac{\partial}{\partial x_j}\left(\mu \frac{\partial \sigma_{ij}}{\partial x_j}\right) - \frac{\partial \overline{\rho}}{\partial x_i} - \frac{\partial \tau_{ij}}{\partial x_j}, \tag{11}$$

where $\sigma_{i,j}$ is the viscous stress tensor, whose components have the form:

$$\sigma_{ij} = \left[\mu\left(\frac{\partial \overline{u_i}}{\partial x_j} + \frac{\partial \overline{u_j}}{\partial x_i}\right)\right] - \frac{2}{3}\mu \frac{\partial \overline{u_i}}{\partial x_i}\delta_{ij}, \tag{12}$$

where μ is the molecular viscosity.

Tensor $\tau_{i,j}$ is called a subgrid stress tensor, and its components are determined by analogy with RANS models from the Boussinesq approximation:

$$\tau_{ij} - \frac{1}{3}\tau_{kk}\delta_{ij} = -2\mu_t \overline{S_{ij}}, \tag{13}$$

Here $\overline{S}_{i,j}$ is strain velocity tensor:

$$\overline{S}_{ij} = \frac{1}{2}\left(\frac{\partial \overline{u_i}}{\partial x_j} + \frac{\partial \overline{u_j}}{\partial x_i}\right), \tag{14}$$

The value μ_t is called the subgrid viscosity. In this paper we used the subgrid viscosity model proposed by Smagorinsky:

$$\mu_t = \rho L_S^2 \dot{\gamma}, \ \left|\overline{S}\right| \equiv \sqrt{2\overline{S_{ij}}\,\overline{S_{ij}}}, \tag{15}$$

where L_s is mixing length of subgrid scales: $L_s = \min\left(kd, C_s V^{1/3}\right)$

Here k is Karman constant, d is the distance to the nearest wall, V is the volume of the computational cell, C_s is the Smagorinsky constant. In the present paper $C_s = 0.17$.

The energy conservation equation for a compressible gas is considered as follows:

$$\frac{\partial \rho E}{\partial t} + \nabla\left(\rho \mathbf{v}(E + p/\rho)\right) = \nabla\left(\lambda_{eff} \nabla T\right), \tag{16}$$

Here E is the total energy, which is defined as:

$$E = h - p/\rho + \mathbf{v}^2/2, \tag{17}$$

In this case, the enthalpy is calculated as:

$$h = \int_{T_0}^{T} C_P(T)\, dT \tag{18}$$

Here $\lambda_{eff} = \lambda + \lambda_t$ – the coefficient thermal conductivity of the mixture, $\lambda_t = \frac{\mu_t C_p}{\mathrm{Pr}_t}$. Here Pr_t is the turbulent Prandtl number equal to 0.85.

The method of solving equations (1)-(9) and the main features of numerical studies are described by *Gavrilov (2011); Minakov et al. (2012, 2015).* The difference analog of the convective-diffusion equations was found using the finite volume method for structured multi-block grids, whose application ensured the persistence of the obtained scheme. To approximate convective terms of the hydrodynamics equations (3), the central difference scheme of second order was used. An implicit first-order scheme was employed to approximate the unsteady terms of the hydrodynamic equations. Diffusion fluxes and source terms were approximated with a second order of accuracy.

The connection between the velocity and pressure fields was realized by SIMPLEC procedure on the combined grids. This approach made it possible to overcome the difficulties described above associated with the resolution of the mobile phase interface. The resulting system of finite-difference equation was solved by an iterative method using a multigrid solver.

Using the described technique, the simulation of water droplet breakup in the flow behind the shock wave was carried out for different Weber numbers within the range of $200 \leq We \leq 2200$. The calculated area was a parallelepiped with dimensions of 3×3×5 cm. The inlet condition with fixed velocity was set on one of the faces of the parallelepiped, determined from the Weber number. On the other faces of the computational domain, free exit conditions were set. At the initial time point, a spherical water droplet with a diameter $d_0 \sim$ 2-3 mm was placed at a distance of 5 mm from the inlet to the computation domain. The droplet was affected by the passing shock wave generating the air flow. The Cartesian uniform computational grid was used in the calculations. The total number of grid nodes was 6.5 million points. However, methodical calculations have shown that such a grid is not enough to resolve the phase interface of the formed small droplets. Therefore, the gradient adaptation technology of the computational grid was applied. With this technology, in the course of calculations, the grid is automatically concentrated in the area of large solution gradients. The gradient of the liquid volume fraction was chosen as the control parameter. An example of how the original grid changes during gradient adaptation for a flow velocity of 60 m/s is shown in Fig. 2. In the field of high gradients, computation cells are four times smaller than those in the initial grid. In the end, the total number of computational nodes of the optimized grid in the course of calculation was approaching 25 million. The use

of such a detailed grid made it possible to resolve secondary droplets up to 20 microns in size.

5. Simulation results and comparison with experiments

The following physical properties of the phases were used in the calculations: water density and viscosity 998.2 kg/m^3 and $1.003 \cdot 10^{-3}$ kg/m·s, surface tension coefficient σ = 0.073 N/m; and air viscosity $1.789 \cdot 10^{-5}$ kg/m·s. To simulate the flow regimes within the range $200 \leq We \leq 2200$, the flow velocity varied from 60 to 170 m/s. The ideal gas model was used.

Figure 3 shows an example of simulating the behavior of a water drop in the flow at We = 208, the Mach number of the shock wave Ms = 1.109, drop size d_0 = 2.73 mm, gas velocity and density u_2 = 60 m/s, ρ_2 = 1.53 kg/m^3, and the time constant $t_0 = (d_0 / u_2) \cdot (\rho_l / \rho_2)^{0.5} \approx 1170$ μs. Fig. 3a corresponds to the period of drop's stay behind the shock wave t_N = 520 μs, as it was in the experiment, while Fig. 3b shows the possible evolution of the drop during the time up to 900 μs as if the quasi-stationary flow behind the shock wave existed so long.

A comparison of the calculation with the experiment at similar points in time is shown in Fig. 4. As can be seen, there is a good qualitative agreement of the data, both in terms of the droplet shape and its deformation dynamics. In addition to the external similarity of the droplet shape, there is a quantitative index of deformation that affects its dynamics, namely, the growth of the droplet cross-section. The dynamics of the droplet midsection growth (d / d_0) is shown in Fig. 5, where a satisfactory agreement of the mean deformation rate in the experiment and calculations is shown.

Figure 6 shows the simulation result of water droplets interaction with shock wave at We = 360, Ms = 1.144, droplet size d_0 = 2.7 mm, gas velocity u_2 = 77 m/s,

density ρ_2 = 1.53 kg/m^3, time constant $t_0 \approx$ 865 μs, the droplet residence time in the flow t_N = 440 μs ($T_N = t_N / t_0$ = 0.47). The beginning of mass entrainment is observed on frames No. 9-10 both in the experiment and the calculations (Fig. 7, b), the breakup induction period $t_i \approx$ 300mks, $T_i = t_i / t_0$ = 0.35.

As can be seen, there is a good qualitative agreement between the numerical simulation and the experimental data at similar time points, but one should not expect complete coincidence of calculations with experiment at a late stage of the process, shown in Fig. 7c. The point is that in the experiment there are circumstantial factors that are difficult to take into account in the calculations. First of all, this concerns the nonsphericity of the droplet due to fluctuations during the separation from the capillary. Here the general picture and rate of deformation are more important since they influence the induction period and the nature of the mass entrainment. As is seen from Fig. 8, the calculated data well describe not only the average deformation rate but also the wave microstructure of the process.

The simulation results of the water droplets interaction with shock wave at We = 650 are shown in Fig. 9. For a droplet with d_0 = 2.73 mm, this is realized at a Mach number of the shock wave Ms = 1.19, gas velocity behind the shock wave front 101 m/s, density ρ_2 = 1.71 kg/m^3, the time constant t_0 = 657 μs. The observation time is t_N = 435 μs when the number of frames N = 15, while the dimensionless value of $T_N = t_N / t_0$ = 0.75 corresponds to the double period induction of mass entrainment, i.e. the beginning of the mass entrainment should be sought on frames No. 7-8, while the time of breakup induction $t_i \approx$ 210-240 μs, $T_i = t_i / t_0$ = 0.35.

The possibility of observing the later stage of the process (T_N = 0.75) allows seeing one more feature, namely, the transverse stretching of the film at the flat bottom

of the drop on frames No. 7-8, which later becomes the mass entrainment zone (Fig. 10c). This also happens with the number We = 360, though not so pronouncedly. At We = 208, the limited observation time T_N in the experiments did not allow observing mass entrainment in general, and that in the bottom region of the droplet, in particular. A comparison of the calculation results with the experimental data obtained at the We = 650 is shown in Fig. 10, which is indicative of good qualitative agreement between the simulation results and experimental data in terms of droplet shape at the characteristic stages of the process. The growth rate of the transverse size of the droplet in Fig. 11 also shows good quantitative agreement with the experiment. It is important to note that not only the average growth rates are close to each other, but similarly, as at We = 360, the phases of surface waves coming to the periphery of the drop coincide. They can be seen by the non-monotonic nature of the growth of the midsection.

Figure 12 shows the numerical simulation result of the interaction of water droplet of d_0 = 2.79 mm with shock wave at We = 2260. This mode is implemented at the Mach number of the shock wave Ms=1.34, the flow velocity behind the shock wave front u_2 = 170 m/s, and the density ρ_2 = 2.04 kg/m^3. In this experiment, the time constant $t_0 \approx$ 362 μs, the beginning of the liquid breakdown falls within the interval between frames No. 5 and 6, i.e. the induction period $t_i \approx$ 135 μs, $T_i = t_i / t_0 = 0.37$.

Figure 13 presents a comparison of the calculation with the experiment on droplet shape, which, as is seen, is quite satisfactory. It is also seen that at the beginning of the mass entrainment (Fig. 13b) microdroplets are observed in front of the windward surface of the mother droplet, excluding only the area near the critical point. This fact deserves special attention and will be discussed in the next section since this type of

breakup is significantly different from the modes at We = 360 and 650, where stripping of the liquid film occurs in the midsection plane and in the bottom region of the drop.

A comparison of the lateral deformation rate of a droplet in the calculations and the experiment in this mode has shown a good agreement up to the interaction time between 100 - 120 microseconds. At the stage of developed mass breakdown, the uncertainty of the drop border against the background of a dense spray does not allow to correctly determine the size of the integral part of the drop in shadow shots, and to verify the calculations by the strain rate.

6. Results and discussion

Table 1 shows the gas-dynamic and other characteristics of the regimes considered, two of which deserve special attention. First, it is the breakup induction period t_i, because it is one of the quantitative indicators to compare calculations with experiments, and secondly, the time constant $t_0 = (d_0 / u_2)\cdot(\rho_l / \rho_2)^{0.5}$ as a generalized parameter of mode of the drop - gas interaction.

The peculiarity of the experiments in shock tubes consists in the limitation of the observation time t_N due to the limited duration of the quasi-stationary flow behind the shock wave, in present experiments $t_N \approx$ 500-600 μs. The *Table* shows that with the increase in the Weber number, the dimensionless time $T_N = t_N / t_0$ increases and covers progressively the later stages of the process, but in the mode with We = 208, the observation time appeared to be insufficient to detect the droplet breakup. Therefore, in the calculations, the "observation" time was extended to 900 μs (Fig. 3b). The time $t_i \approx$ 600 μs is obtained from the calculated "visualization", while the dimensionless time $T_i = t_i / t_0$ appears to be slightly overstated in comparison with other modes. This is due to the fact that the regime with We ≈ 200 is in the transition region between Rayleigh-

Taylor instability and stripping mechanisms, while at We < 200 the breakup delay increases and reaches the value of $T_i \approx 2$ by *Dai et al. (2001).* The transition region is characterized by the simultaneous development of several breakup mechanisms, and thus the process is called a mixed or multimode regime *Dai et al. (2001).* In this example, this type of deformation is typical for the "sheet stripping" mechanism at an early stage of interaction (Fig. 3a), and the development of Rayleigh-Taylor waves at a late stage (Fig. 3b).

As for the other modes, the calculations have shown a good agreement of the induction period t_i with the experiments. The dimensionless induction time is independent of the We number and equals to $T_i = \text{const} \approx 0.36$. Then, for estimates of the drop breakup delay at We > 250, an empirical formula can be used $t_i = 0.36 \cdot (d_0 / u_2) \cdot (\rho_l / \rho_2)^{0.5}$**,** the velocity u_2 and density ρ_2 of the gas is computed as a function of Mach number of the shock wave Ms in *Henshall (1957); Lapworth (1970).*

The second quantitative factor to verify the calculation is deformation dynamics. In calculations and experiments, the average growth rate of the drops mid-section is very close, and its non-monotonic character is noted. In *Boiko et al. (2012)* this was explained by the arrival of concentric surface waves to the equator of a droplet, though at We = 208 there is a divergence of the waves phase (Fig. 5). This may be due to the initial non-sphericity of the droplet at the time of impact by the shock wave. In other modes, the phases of surface waves in the calculations and experiments coincide with high accuracy (Figs.8 and 11). Thus, the comparison of numerical simulation with the experiment has shown good agreement in terms of the droplet shape, deformation dynamics, and breakup delay that indicates a high-resolution capability of the computational algorithm.

Given the known data on the time of complete breakup of the droplet $t / t_0 = T \approx 5$ by *Gelfand et al. (1974); Dai et al. (2001)* we note that in this paper, only the early stage ($T_i < T_N < T$) is considered, though it is very important for understanding the processes occurring inside and outside the droplet. Although the problem of internal processes is not set here, it is useful to highlight the main issues: these are "macroscopic" movement of the liquid during drop deformation, the development of the conjugated boundary layer, and surface instability. These are hidden processes that are not observable and can be judged only indirectly by the nature of the drop deformation and picture of it flow around.

The relationship between the droplet shape and the streamlining pattern is seen in the response of the liquid sphere to the change in the velocity field near it. That is, to understand the evolution of the droplet shape, a general picture of the flow pattern is necessary, but panoramic methods of velocity measurements, such as for example, PIV, are not applicable in shock tube because of the operation speed limitation. Therefore, in *Boiko et al. (2012)* experiments were carried out with the droplet model in a stationary flow at the Reynolds number $Re \sim 10^3$-10^4, equal to that in a shock wave. The model had the shape typical to one at the initial stage of droplet breakdown (Figs. 4b, 7b, 10b, and 13b). The features of the flow around such a body according to PIV data will be considered later, while here we will focus on the first important observations on the results of numerical simulation of the flow around the drop at different stages of its shape evolution.

So in Fig. 14, the flow pattern for the mode in Fig. 3 is shown (We = 208). When the droplet is slightly deformed, the flow around it is close to the flow around the sphere at the corresponding Reynolds numbers ($Re \sim 10^3$-10^4) with a vortex separation

near the midsection (1). Then, 200 μs after a drop enters the flow, a toroidal vortex (2) and a reverse flow (3) are formed simultaneously with the generation of two annular waves (4) and (5) on the initially spherical droplet. This type of deformation is typical for the entire investigated range of Weber numbers. The analysis of the gas velocity field, performed in *Boiko et al. (2012)*, revealed the features of the flow around such a body, which are given below, and it remains to be noted that all of them can be traced in the results of numerical simulation (Fig.14).

Thus, the external flow is unsteady, but it contains several constant gas-dynamic structures, whose behavior and their effect on the drop can be interpreted as follows:

- The first higher wave (fracture of the generatrix) is generated even at the spherical shape of the droplet at the point of flow separation, where its velocity is maximal (red region), while the pressure is minimal. The recirculation zone with a counter-current flow along the droplet surface (area *1*) is visible behind the separation point. In the conjugated boundary layer, the liquid moves to the midsection which along with decreased pressure contributes to the growth of the latter.
- The second stationary structure is in the droplet wake and represents a second recirculation zone with intense reverse flow along the wake axis (area *3*). The pressure distribution in the bottom of the droplet caused by this impact flow makes the surface flat and the nature of the gas movement is radial spreading over the bottom surface.
- Here the second fracture of the generatrix is formed, which is associated with the radial spreading of the liquid over the bottom surface. As can be seen in Figs. 6, 9, and 12, this leads to the formation of a liquid disk, whose edge supplies the droplet crushing products to the aerodynamic wake.

- Spreading radially over the bottom surface, the gas flow is separated near the second wave (***5***). At that, part of it penetrates into the first separation zone (***1***) along the droplet surface, while the rest of the flow enters the third permanent structure (***2***) (Fig.15).
- The structure (***2***) partially separates the first two ones and is an isolated toroidal vortex. Without interacting with the droplet surface, it originates at its bottom part and drifts into aerodynamic track at a speed much less than the speed of the oncoming flow.
- Comparison of shadow images of the droplet at the beginning of the breakup with the external flow field has shown that the mass breakdown occurs from the wave crests, i.e. annular fractures of the generatrix, while they are formed at the flow separation points (***4***) and (***5***) shown in Fig.14.

This type of drop breakup corresponds to the "sheet stripping" mechanism, and its features are visible at the modes with We = 208, 360, and 650. In the modes with We > 2000, the droplet morphology is similar to the previous examples, but the mass breakdown occurs not only from the edges of the two main waves. At We = 2260, the presence of breakup products in front of the windward surface of the droplet was noted (Fig.13b). These daughter droplets originated due to the wave crest stripping as well, though waves were of a different scale and nature. These are Kelvin-Helmholtz instability waves on the windward surface of the droplet. The attributes of their stripping shown in Fig.13b are perhaps the only evidence of the change in breakup mechanism within this range of modes described in B*oiko et al. (2012)* and obtained in the calculations. Note also that the restriction of the grid size (~ 20 μm) does not allow

for resolving smaller daughter droplets, otherwise there would be substantially more of them.

Figure 15 presents the calculated velocity field near the droplet at We = 2260, from which the same structures are visible as at We = 208, namely, the flow separation region (***1***) at the point with maximum velocity (red region) and minimum pressure, an isolated solitary toroidal vortex (***2***), and the reverse flow on the wake axis (***3***). At the time point equal to 70 μs, a scheme of the bottom flow separation into two vortices (***1***) and (***2***) is shown that was described in *Boiko et al. (2012)* for the solid model. The signs of structures (***1***) and (***2***) are visible until the interaction time ≈ 120 μs, and further the flow in the wake loses its axial symmetry and disintegrates into small non-stationary structures. They form a large stagnant area with a low average velocity comparable to the velocity in the flow deceleration zone in front of the windward surface of the drop.

And finally, the last remark: the external current lines are closed in the far wake of the drop at a greater distance than that of the sphere, since they cover not only the drop itself, but also the extensive vortex structures provoked by the breaks of the generatrix on the deformable surface. This can be seen in Fig. 15 of the flow field at instants of 32 μs and 70 μs. Thus, the results of the flow field simulation near a deformable drop are in many ways consistent with the PIV data for a solid model with a similar shape and advance in understanding an overall picture of the drop behavior in the shock wave and hidden processes inside it.

Conclusions

Experimental investigation and numerical simulation of water drop interaction with the flow behind incident shock wave within the range of Weber numbers We = 208 – 2260 were performed. A comparison of the numerical simulation results with

experimental data on the droplets morphology, deformation dynamics, and breakup induction time has shown a good agreement for all modes that indicates a high-resolution capability of the computational algorithm. The flow structure near the drop and in its wake at various stages of deformation was studied, the features of flow around droplet that define the type of droplet shape evolution and the nature of breakdown were considered. The complex of experimental data and numerical simulation results provided the basis for constructing a phenomenological picture of the water drop behavior in the flow behind incident shock wave.

Acknowledgments

The research was carried out within the framework of the Program of Fundamental Scientific Research of the state academies of sciences in 2013-2020 (project No. AAAA- A17-117030610137-0) and partly supported by RFBR (project No. 18-38-00565).

References

Aggarwal S.K., Peng F., 1995. A review of droplet dynamics and vaporization modeling for engineering calculations. J. Eng. Gas Turbines Power. 117. 453–461.

Boiko V.M., Kiselev V.P., Kiselev S.P., Papyrin A.N., Poplavsky S.V., Fomin V.M. 1997. Shock wave interaction with a cloud of particles. Shock Waves. 7. 275-285

Boiko V.M., Lotov V.V., Papyrin A.N., 1991. Ignition of liquid fuel drops in shock waves. Dynamics of deflagrations and reactive systems: heterogeneous combustion. Progress in Astron. Aeron. 132. 205-219.

Boiko V.M., Papyrin A.N., Poplavski S.V., 1987. Dynamics of droplet breakup in shock waves. J. of Applied Mechanics and Technical Physics. 28 (2). 263–269.

BoikoV.M., Papyrin A.N., Poplavski S.V., 1993. Mechanism of dust ignition in incident shock waves. Combustion Explosion and Shock Waves. 29 (3). 389-394.

Boiko V.M., Poplavski S.V., 2012. Experimental study of two types of stripping breakup of a drop in the flow behind the shock wave. Combustion Explosion and Shock Waves. 48 (4). 440-445. doi:10.1134/S0010508212040107.

Boiko V.M., Poplavski S.V., 2009. On the dynamics of droplet acceleration at the early stage of velocity relaxation in the shock wave. Combustion Explosion and Shock Waves. 45 (2). 198-204. doi: 10.1007/s10573-009-0026-4.

Boiko V.M., Poplavskii S.V., 2007. Particle and drop dynamics in the flow behind a shock wave. Fluid Dynamics, 42 (3). 433–441. doi: 10.1134/S0015462807030118.

Boiko V.M., Poplavski S.V., 2002. Self-ignition and ignition of aluminum powders in shock waves Shock Waves.11. 289–295

Brackbill J.U., Kothe D.B., Zemach C.A., 1992. Continuum method for modeling surface tension. J. Comput. Phys. 100. 335– 354. doi:10.1016/0021-9991(92)90240-Y.

Dai Z., Faeth G.M., 2001. Temporal properties of secondary drop breakup in the multimode breakup regime. International Journal of Multiphase Flow. 27. 217-236. doi: 10.1016/S0301-9322(00)00015-X.

Dinh T.N., Li G.J., Theofanous T.G., 2003. An investigation of droplet breakup in a high Mach, low Weber number regime. 41st AIAA Aerospace Sciences Meeting and Exhibit, January 6–9, Reno, NV. doi: 10.2514/6.2003-317.

Frank A. M., 2001. Discrete model of incompressible fluid. Moscow, Fizmatlit. 206.

Gavrilenko T.P., Grigoriev V.V., Zhdan S.A., Nicolaev Y.A., Boiko V.M., Papyrin A.N., 1986. Acceleration of Solid Particles by Gaseous Detonation Products. Combustion and Flames.66 (2). 121-128.

Gavrilov A.A., Dekterev A.A., Minakov A.V., Rudyak V.Y., 2011. A numerical algorithm for modeling laminar flows in an annular channel with eccentricity. J. of Applied and Industrial Mathematics. 5 (4). 559-568. doi:10.1134/S1990478911040119.

Gelfand B.E., 1996. Droplet breakup phenomena in flows with velocity lag. Progr. Energy Combust. Sci. 22 (3). 201–265. doi: 10.1016/S0360-1285(96)00005-6.

Gelfand B.E., Gubin S.A., Kogarko S.M., 1974. Main modes of droplet breakup in shock waves and their characteristics. J. of engineering physics, 27 (1). 119-126.

Gelfand B.E., Gubin S.A., Timofeev I.U., Sheparnev S.M., 1978. Desintagration of liquid drop aggregation in shock waves. J. of Applied Mechanics and Technical Physics 6. 43-48.

Henshall B.D., 1957. On some aspects of the use of shock tubes in aerodynamic research. ARS Rep. & Memor. 3044, Univ. Bristol, Dept. Aeronaut. Eng., London

Hirt C.W, Nichols B.D., 1981. Volume of fluid (VOF) method for the dynamics of free boundaries // Journal of computational physics. 39. 201-226.

Kothe D.B., Rider W.J., 1996. Volume tracking of interfaces having surface tension in two and three dimensions. S.J. AIAA. 96.

Lapworth K.C., 1970. Normal shock-wave tables for air, argon, carbon dioxide and oxygen. london: her majesty's stationery office. Current Papers C.P. 1101. 30.

Minakov A.V., 2014. Numerical algorithm for moving boundary fluid dynamics problems and its testing. Computational Mathematics and Mathematical Physics. 54 (10). 1560-1570. doi: https://doi.org/10.7868/S0044466914100111.

Minakov A.V., Pervukhin M.V., Platonov D.V., Khatsayuk M.Y., 2015. Mathematical model and numerical simulation of aluminum casting and solidification in magnetic fields with allowance for free surface dynamics. Computational Mathematics and Mathematical Physics. 55 (12) 2066-2079. doi: 10.1134/S096554251512009X.

Minakov A.V., Rudyak V.Y., Gavrilov A.A., Dekterev A.A., 2012. Mixing in a T-shaped micromixer at moderate Reynolds numbers. Thermophys. Aeromech. 19. 385–395.

Ortiz C., Joseph D.D., Beavers G.S., 2004. Acceleration of a liquid drop suddenly exposed to a high-speed airstream. International Journal of Multiphase Flow. 30 (2). 217-224. doi:10.1016/j.ijmultiphaseflow.2003.11.004.

Ranger A.A., Nicholls J.A., 1969. The aerodynamic shattering of liquid drops. AIAA Journals. 7 (2). 285-290. doi:10.2514/3.5087.

Ranger A.A., Nicholls J.A., 1970 Shape and surrounding flowfield of a drop in a high-speed gas stream. AIAA Journals. 8 (9). 1720-1722.

Smagorinsky J., 1963. General Circulation Experiments with the Primitive Equations. I. The Basic Experiment. Month. Wea. Rev. 91. 99–164.

Tavangar S., Hashemabadi S.H., Saberimoghadam A., 2015. CFD simulation for secondary breakup of coal-water slurry drops using Open FOAM. Fuel Processing Technology. 132.153–163.

Theofanous T.G., Li G.J., 2008. On the physics of aerobreakup. Physics of Fluids. 20. 052103.

Versluis M., 2013. High-speed imaging in fluids. Exp Fluids. 54 (1458). 1-35.

Table 1

We	M_S	u_2, m/s	ρ_2, kg/m^3	t_0, μs	$T_N = t_N/t_0$	t_i, μs	$T_i = t_i/t_0$
208	1.109	59.8	1.53	1168	0.4	*600*	0.5
360	1.144	77.9	1.61	865	0.47	330	0.36
653	1.19	101	1.71	657	0.96	220	0.35
2000	1.32	162	2.0	387	1	142	0.36
2260	1.34	170	2.04	362	1	135	0.37

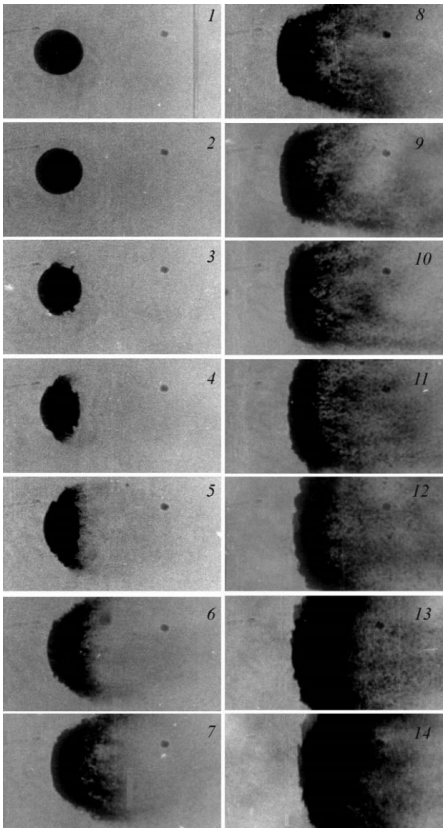

Fig. 1. Shadow images of the water droplet interaction with incident shock wave; We = $2 \cdot 10^3$, the frames spacing $30 \cdot 10^{-6}$ s.

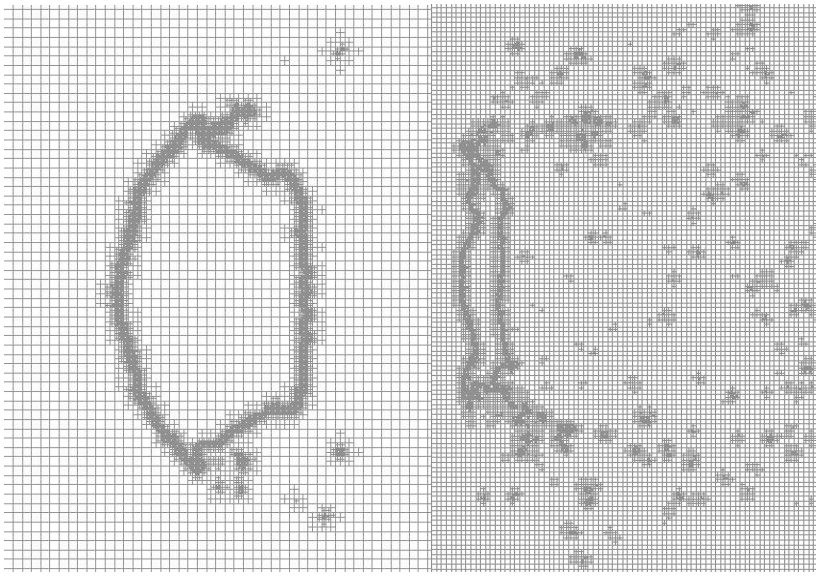

Fig. 2. Evolution of the computational grid near the phase interface by means of gradient adaptation.

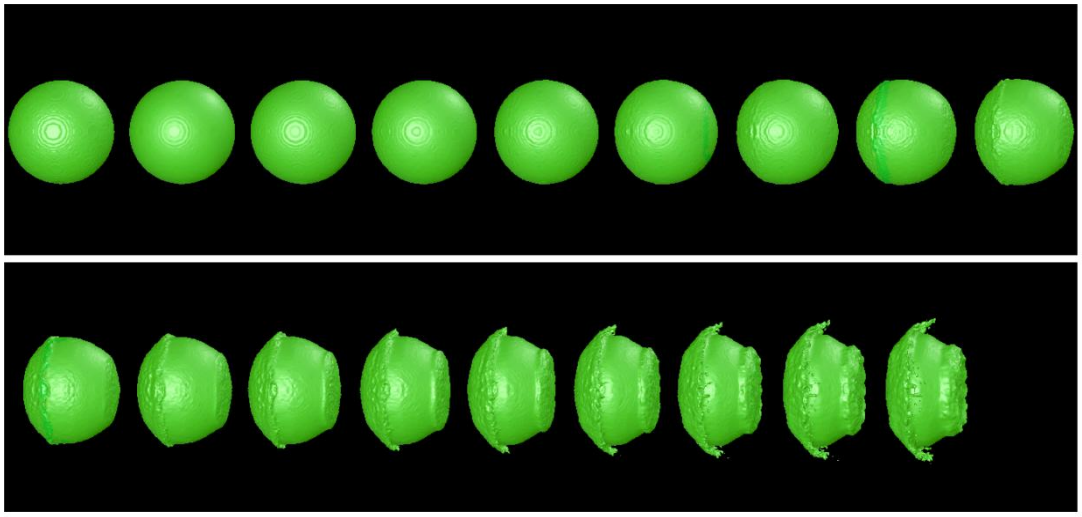

a)

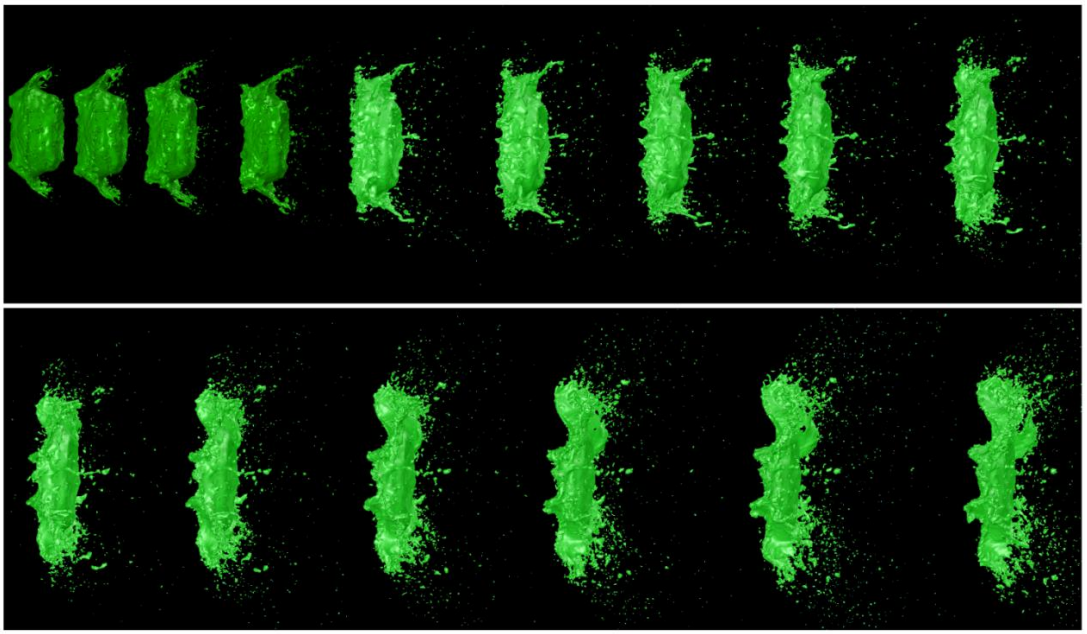

b)

Fig. 3. Numerical simulation of the water drop behavior behind incident shock wave at We=208;
a) period up to 520 μs, b) period of 550 - 900 μs.

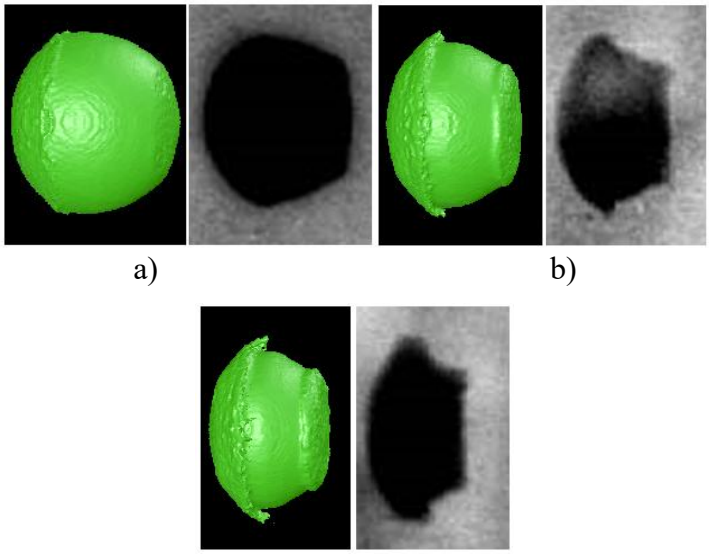

a) b)

c)

Fig. 4. Comparison of calculation with experimental data on the droplet shape at We = 208;
a) 240 μs; b) 360 μs; c) 420 μs.

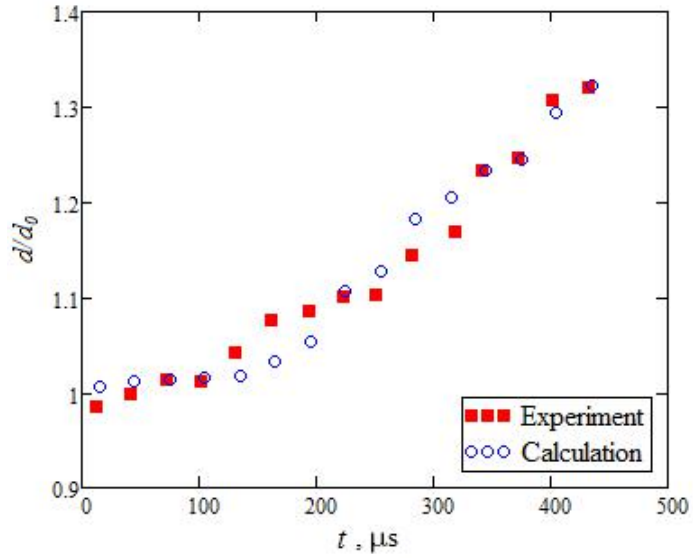

Fig. 5. The transverse deformation rate of a water drop at We = 208.

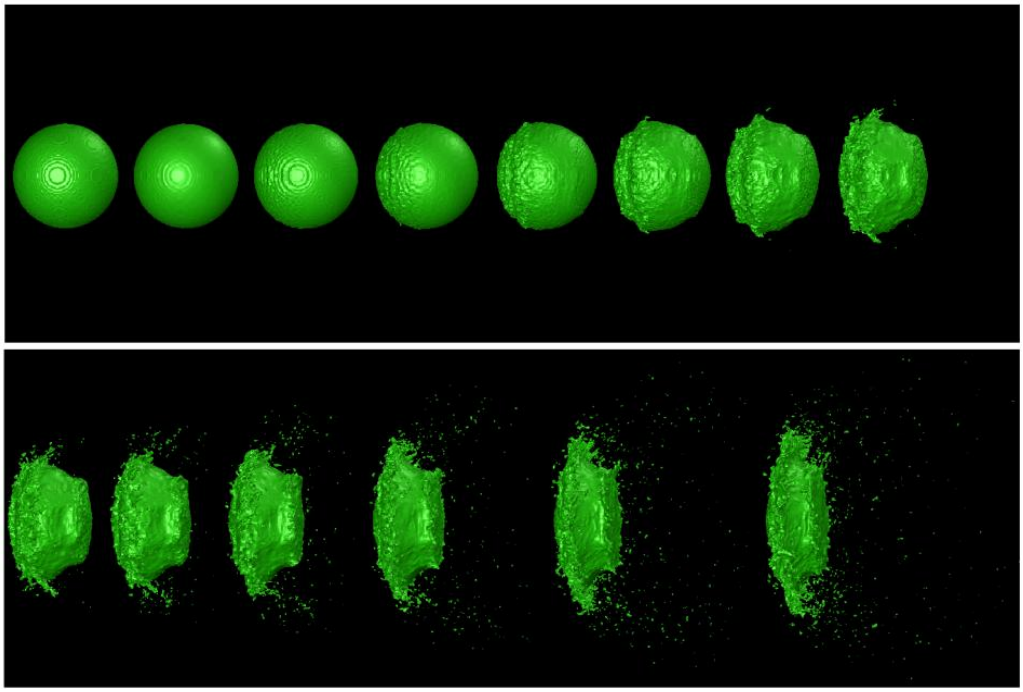

Fig. 6. The breakup of water droplets behind the shock wave at Ms = 1.144, We = 360.

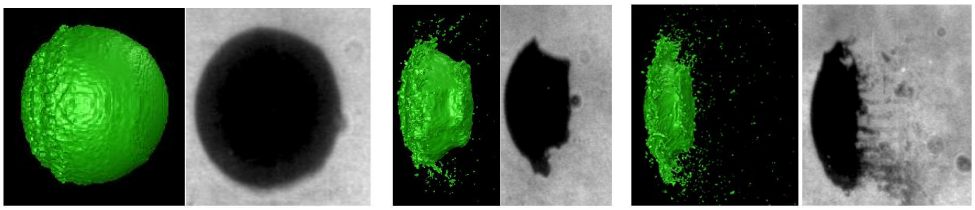

a) b) c)

Fig. 7. Comparison of calculation results with experimental data for We = 360 at the following time points: 120 μs (a), 300 μs (b), 390 μs (c).

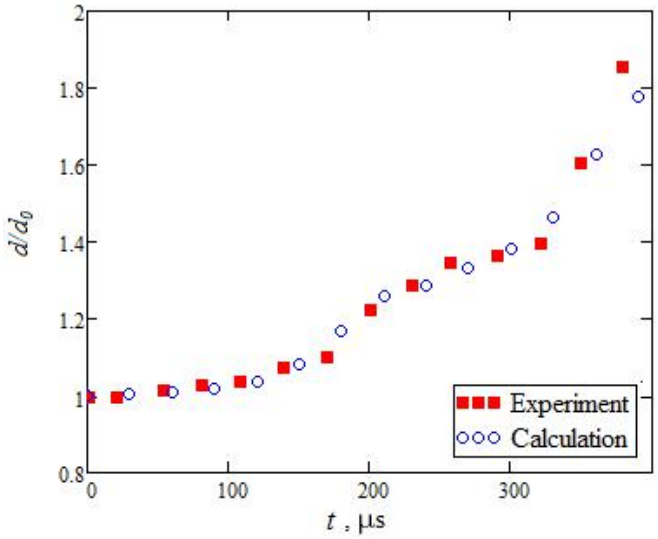

Fig. 8. The water droplet deformation rate at We = 360.

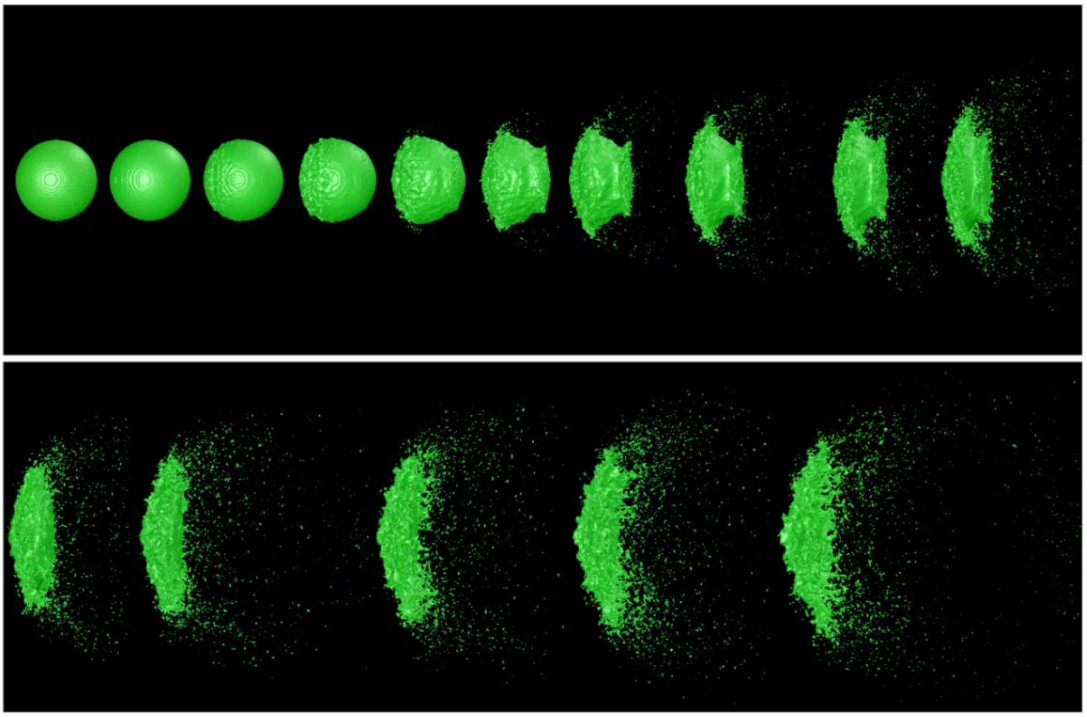

Fig. 9. The behavior of water droplet behind incident shock wave at Ms = 1.19, We = 650.

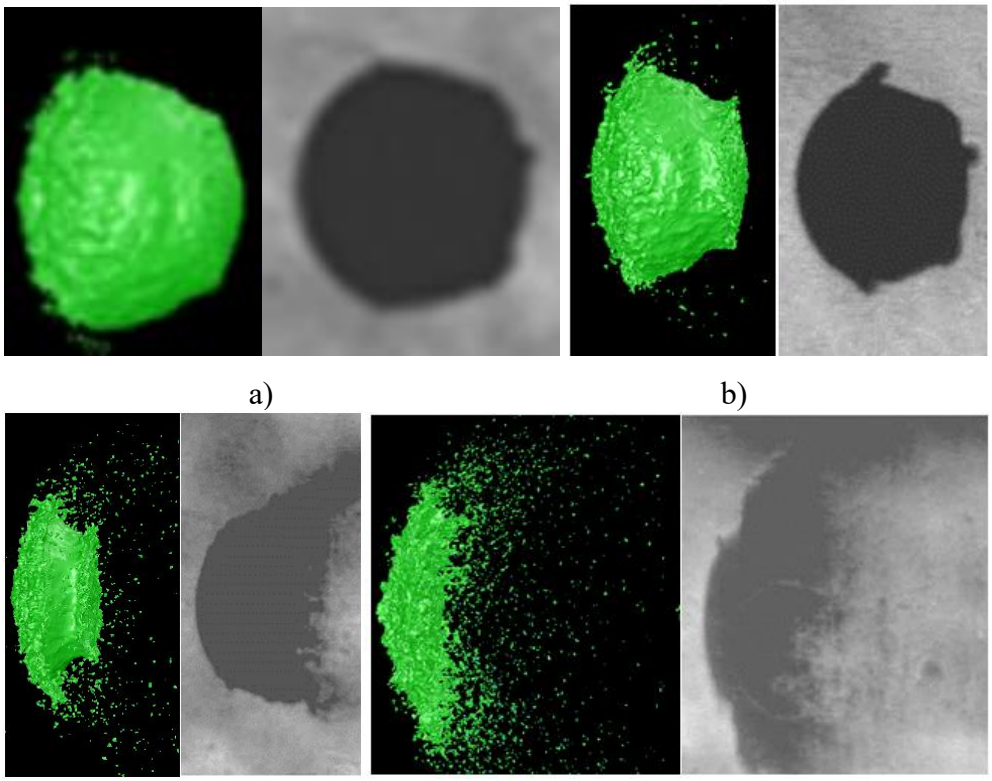

a) b)

c) d)

Fig. 10. Comparison of the droplet shape in the calculation and experiment at We = 650; a) 120 μs; b) 150 μs; c) 240 μs; d) 390 μs.

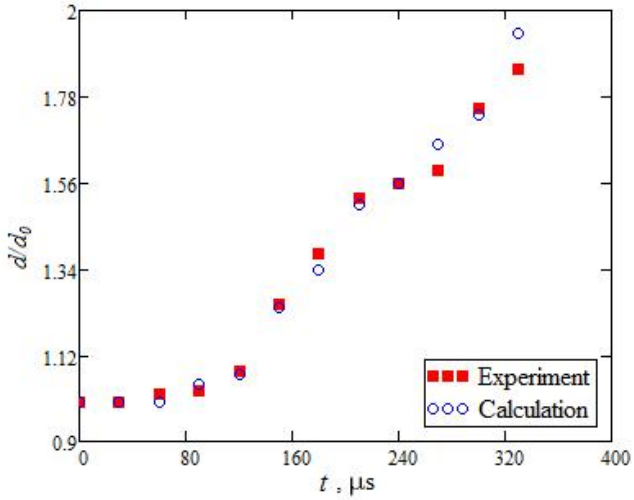

Fig. 11. The deformation rate of water droplet behind the shock wave at We = 650.

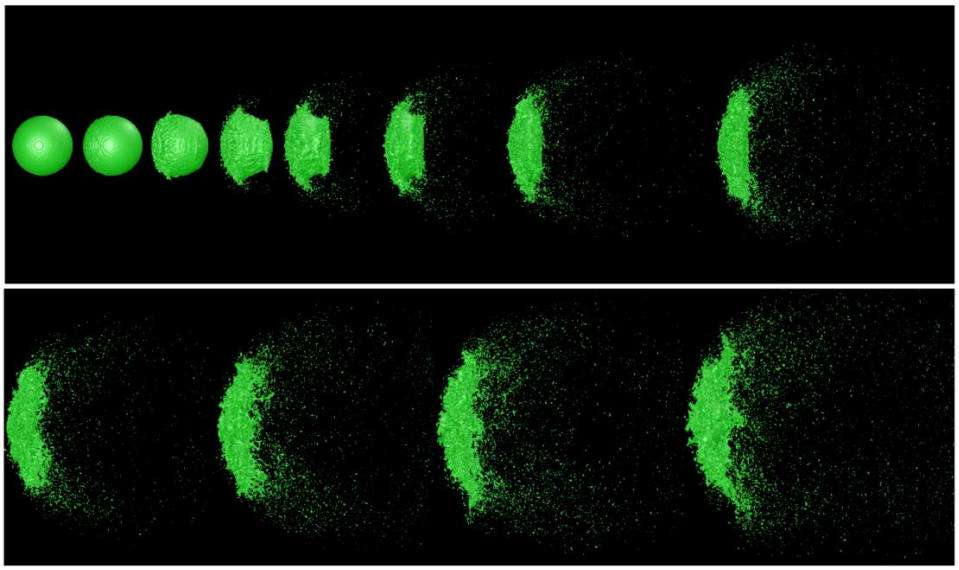

Fig. 12. Water droplet breakup dynamics behind the shock wave at We = 2260.

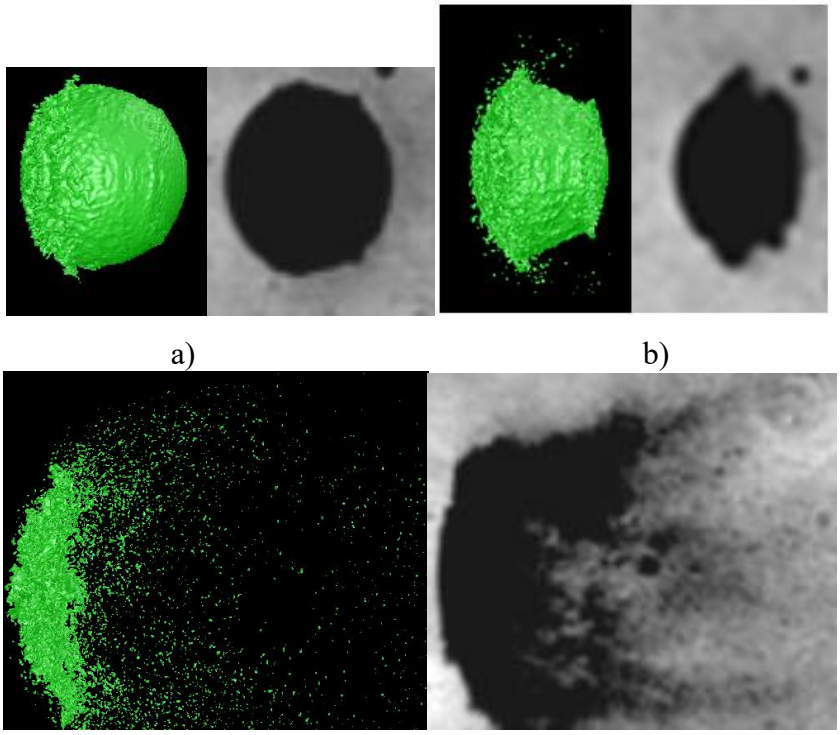

Fig. 13. Comparison of calculation with experiment in the form of drop at We = 2260; a) 60 μs, b) 90 μs, c) 270 μs.

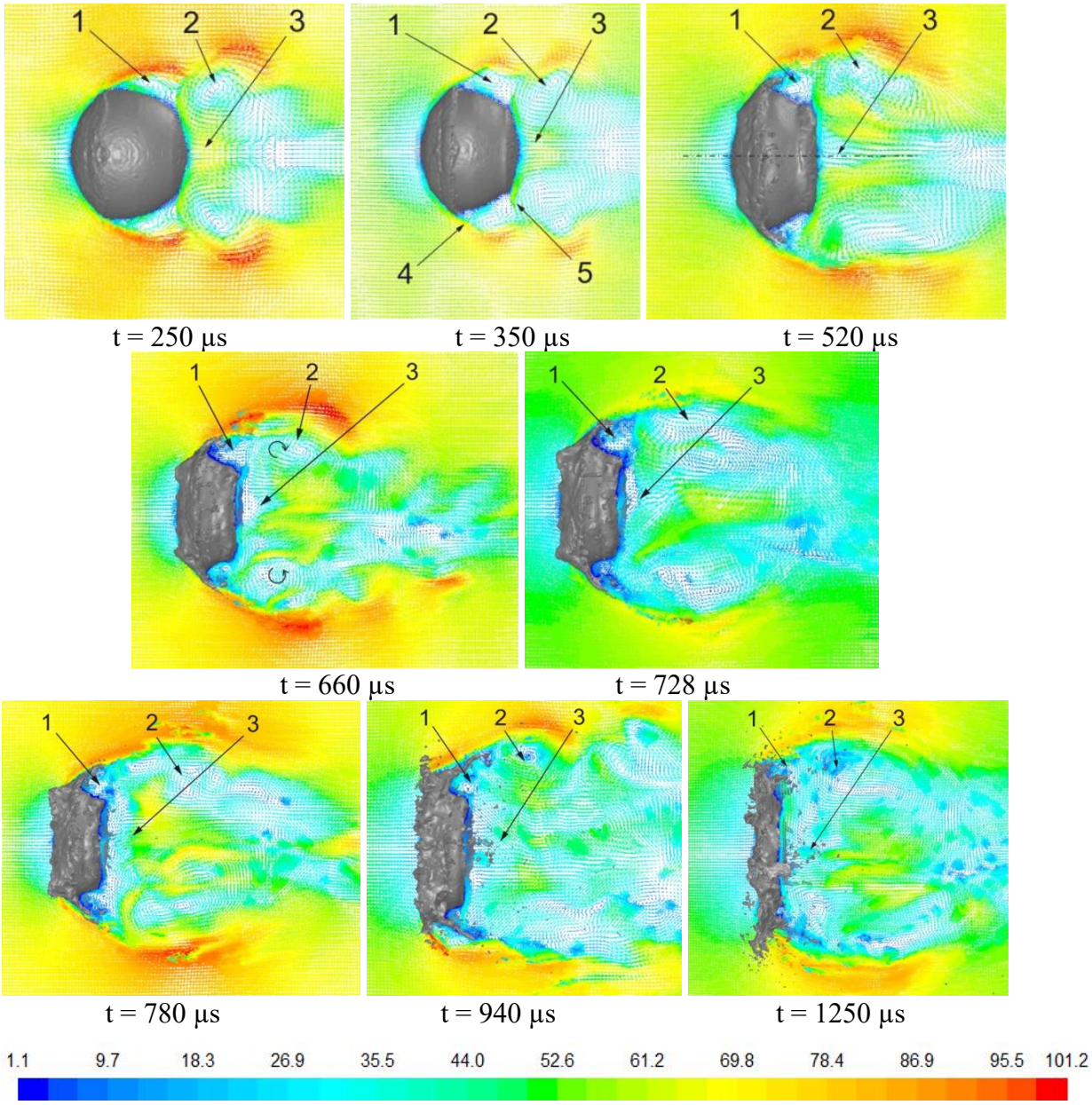

Fig. 14. The flow field near a drop and in its wake at different time points, We = 208;
1 – toroidal vortex in the flow separation region; 2 – solitary toroidal vortex;
3 – return flow near the wake axis; 4 – fracture of generatrix at the point of flow separation; 5 – fracture of generatrix in the bottom of the drop.

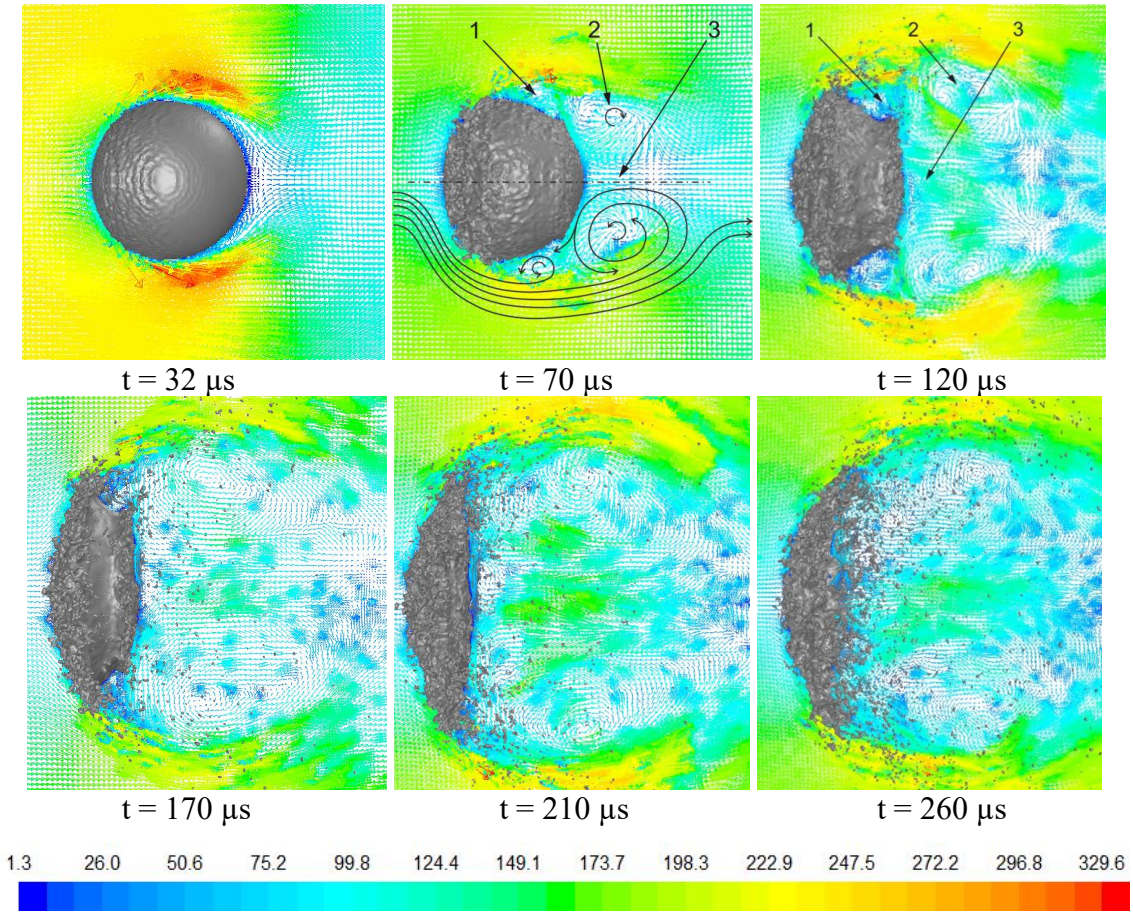

Fig. 15. The flow field near and in the wake of a drop at different time points for We = 2260; 1 – toroidal vortex in the flow separation region, 2 – solitary toroidal vortex, 3 – reverse flow near the wake axis.